The Astrophysical Journal Letters, 901:L8 (12pp), 2020 September 20 https://doi.org/10.3847/2041-8213/abb3be

Molecular Gas Properties on Cloud Scales across the Local Star-forming Galaxy Population

Jiayi Sun (孙嘉懿)[1], Adam K. Leroy[1], Eva Schinnerer[2], Annie Hughes[3,4], Erik Rosolowsky[5], Miguel Querejeta[6,7], Andreas Schruba[8], Daizhong Liu[2], Toshiki Saito[2], Cinthya N. Herrera[9], Christopher Faesi[2,10], Antonio Usero[7], Jérôme Pety[9,11], J. M. Diederik Kruijssen[12], Eve C. Ostriker[13], Frank Bigiel[14], Guillermo A. Blanc[15,16], Alberto D. Bolatto[17], Médéric Boquien[18], Mélanie Chevance[12], Daniel A. Dale[19], Sinan Deger[20], Eric Emsellem[6,21], Simon C. O. Glover[22], Kathryn Grasha[23], Brent Groves[23], Jonathan Henshaw[2], Maria J. Jimenez-Donaire[7,24], Jenny J. Kim[12], Ralf S. Klessen[22,25], Kathryn Kreckel[12], Janice C. Lee[20], Sharon Meidt[26], Karin Sandstrom[27], Amy E. Sardone[1,28], Dyas Utomo[1], and Thomas G. Williams[2]

[1] Department of Astronomy, The Ohio State University, 140 West 18th Avenue, Columbus, OH 43210, USA; Sun.1608@osu.edu
[2] Max-Planck-Institut für Astronomie, Königstuhl 17, D-69117 Heidelberg, Germany
[3] CNRS, IRAP, 9 Av. du Colonel Roche, BP 44346, F-31028 Toulouse cedex 4, France
[4] Université de Toulouse, UPS-OMP, IRAP, F-31028 Toulouse cedex 4, France
[5] Department of Physics, University of Alberta, Edmonton, AB T6G 2E1, Canada
[6] European Southern Observatory, Karl-Schwarzschild Straße 2, D-85748 Garching bei München, Germany
[7] Observatorio Astronómico Nacional (IGN), C/Alfonso XII, 3, E-28014 Madrid, Spain
[8] Max-Planck-Institut für extraterrestrische Physik, Giessenbachstraße 1, D-85748 Garching, Germany
[9] Institut de Radioastronomie Millimétrique (IRAM), 300 Rue de la Piscine, F-38406 Saint Martin d'Hères, France
[10] Department of Astronomy, University of Massachusetts Amherst, 710 North Pleasant Street, Amherst, MA 01003, USA
[11] Sorbonne Université, Observatoire de Paris, Université PSL, CNRS, LERMA, F-75014 Paris, France
[12] Astronomisches Rechen-Institut, Zentrum für Astronomie der Universität Heidelberg, Mönchhofstraße 12-14, D-69120 Heidelberg, Germany
[13] Department of Astrophysical Sciences, Princeton University, Princeton, NJ 08544 USA
[14] Argelander-Institut für Astronomie, Universität Bonn, Auf dem Hügel 71, D-53121 Bonn, Germany
[15] Observatories of the Carnegie Institution for Science, 813 Santa Barbara Street, Pasadena, CA 91101, USA
[16] Departamento de Astronomía, Universidad de Chile, Camino del Observatorio 1515, Las Condes, Santiago, Chile
[17] Department of Astronomy, University of Maryland, College Park, MD 20742, USA
[18] Centro de Astronomía (CITEVA), Universidad de Antofagasta, Avenida Angamos 601, Antofagasta, Chile
[19] Department of Physics and Astronomy, University of Wyoming, Laramie, WY 82071, USA
[20] Infrared Processing and Analysis Center (IPAC), California Institute of Technology, Pasadena, CA 91125, USA
[21] Univ Lyon, Univ Lyon 1, ENS de Lyon, CNRS, Centre de Recherche Astrophysique de Lyon UMR5574, F-69230 Saint-Genis-Laval, France
[22] Universität Heidelberg, Zentrum für Astronomie, Institut für Theoretische Astrophysik, Albert-Ueberle-Str 2, D-69120 Heidelberg, Germany
[23] Research School of Astronomy and Astrophysics, Australian National University, Canberra, ACT 2611, Australia
[24] Harvard-Smithsonian Center for Astrophysics, 60 Garden Street, Cambridge, MA 02138, USA
[25] Universität Heidelberg, Interdisziplinäres Zentrum für Wissenschaftliches Rechnen, Im Neuenheimer Feld 205, D-69120 Heidelberg, Germany
[26] Sterrenkundig Observatorium, Universiteit Gent, Krijgslaan 281 S9, B-9000 Gent, Belgium
[27] Center for Astrophysics and Space Sciences, Department of Physics, University of California, San Diego, 9500 Gilman Drive, La Jolla, CA 92093, USA
[28] Center for Cosmology and Astroparticle Physics, The Ohio State University, 191 West Woodruff Avenue, Columbus, OH 43210, USA
Received 2020 July 25; revised 2020 August 25; accepted 2020 August 27; published 2020 September 18

Abstract

Using the PHANGS–ALMA CO(2–1) survey, we characterize molecular gas properties on ∼100 pc scales across 102,778 independent sightlines in 70 nearby galaxies. This yields the best synthetic view of molecular gas properties on cloud scales across the local star-forming galaxy population obtained to date. Consistent with previous studies, we observe a wide range of molecular gas surface densities (3.4 dex), velocity dispersions (1.7 dex), and turbulent pressures (6.5 dex) across the galaxies in our sample. Under simplifying assumptions about subresolution gas structure, the inferred virial parameters suggest that the kinetic energy of the molecular gas typically exceeds its self-gravitational binding energy at ∼100 pc scales by a modest factor (1.3 on average). We find that the cloud-scale surface density, velocity dispersion, and turbulent pressure (1) increase toward the inner parts of galaxies, (2) are exceptionally high in the centers of barred galaxies (where the gas also appears less gravitationally bound), and (3) are moderately higher in spiral arms than in inter-arm regions. The galaxy-wide averages of these gas properties also correlate with the integrated stellar mass, star formation rate, and offset from the star-forming main sequence of the host galaxies. These correlations persist even when we exclude regions with extraordinary gas properties in galaxy centers, which contribute significantly to the inter-galaxy variations. Our results provide key empirical constraints on the physical link between molecular cloud populations and their galactic environment.

Unified Astronomy Thesaurus concepts: Millimeter astronomy (1061); Molecular gas (1073); Late-type galaxies (907)

Supporting material: machine-readable tables

1. Introduction

Observations indicate that the physical properties of giant molecular clouds (GMCs) vary systematically with their location in a galaxy. This result is obtained in the Milky Way (e.g., Rice et al. 2016; Roman-Duval et al. 2016; Miville-Deschênes et al. 2017; Colombo et al. 2019, but see Lada & Dame 2020) and in other galaxies (e.g., Donovan Meyer et al. 2013; Hughes et al. 2013a; Colombo et al. 2014a; Leroy et al. 2016; Schruba et al. 2019). This suggests that GMCs are connected to their galactic context, which affects their formation, structure, or evolution (see, e.g., Field et al. 2011; Hughes et al. 2013a; Jeffreson & Kruijssen 2018; Meidt et al. 2018, 2020; Schruba et al. 2019; Sun et al. 2020).

Understanding this cloud–environment connection has been a challenge because it requires comprehensive, observationally expensive mapping of GMC demographics across the local galaxy population. This challenge is being addressed by PHANGS–ALMA,[29] a large CO (2–1) line survey covering essentially all ALMA-visible, nearby, massive, star-forming galaxies (A. K. Leroy et al. 2020a, in preparation). PHANGS–ALMA well samples the local star-forming main sequence across two decades in stellar mass (10^9–$10^{11}\,M_\odot$). The high resolution and sensitivity of the PHANGS–ALMA data offer an unprecedented opportunity to characterize molecular gas properties on 50–150 pc "cloud scales," and the cloud–environment connection across typical star-forming environments in the local universe.

In this Letter, we report measurements of the cloud-scale molecular gas surface density and velocity dispersion, as well as estimates of the turbulent pressure and the virial parameter. Following our analysis of the PHANGS–ALMA pilot sample of 11 galaxies (Sun et al. 2018, hereafter S18), we derive these measurements on fixed 90 pc and 150 pc scales using the full PHANGS–ALMA survey, which increases our sample size to 70 galaxies. The derived measurements constitute a benchmark data set that can be readily compared with observations of other types of galaxies or numerical simulations reaching similar spatial resolutions (e.g., Semenov et al. 2018; Dobbs et al. 2019; Fujimoto et al. 2019; Jeffreson et al. 2020).

2. Data and Measurements

Overview: We carry out a pixel-by-pixel analysis of molecular gas properties at fixed 90 pc and 150 pc scales. This method provides a simple, reproducible characterization of all detected emission (e.g., Sawada et al. 2012; Hughes et al. 2013b; Leroy et al. 2016). Complementary analyses decomposing the same CO data into individual objects (E. Rosolowsky et al. 2020, in preparation; A. Hughes et al., in preparation) yield qualitatively similar conclusions.

Galaxy sample: We include the 70 PHANGS–ALMA galaxies that had fully processed ALMA data by 2019 December.[30] They consist of 67 out of the 74 galaxies in the ALMA Large Program and pilot samples and three nearby galaxies from the extended PHANGS–ALMA sample. Table A1 lists the galaxy sample together with their global properties (columns 1–9).

Data characteristics: The PHANGS–ALMA CO (2–1) data have native spatial resolutions of 50–150 pc at the distances of the target galaxies, and 1σ noise levels of 0.2–0.3 K per 2.5 km s^{-1} channel. They combine ALMA interferometric array and single-dish observations to recover emission across the full range of spatial scales (see A. K. Leroy et al. 2020b, in preparation).

Data homogenization: We convolve the data cubes to a common 150 pc spatial resolution to allow direct comparison between all 70 galaxies. For a subset of 35 galaxies, we are also able to convolve the cubes to 90 pc resolution to investigate trends with spatial resolution (see also S18).

Product creation: We mask the data cubes to only include voxels that contain emission detected with high confidence.[31] We integrate the masked cubes along the spectral axis to produce the integrated intensity ($I_{\rm CO}$) and effective line width ($\sigma_{\rm CO}$) maps. The latter quantity is derived as $\sigma_{\rm CO} = I_{\rm CO}/(\sqrt{2\pi}\ T_{\rm peak})$ following Heyer et al. (2001),[32] where $T_{\rm peak}$ is the brightness temperature at the line peak, and is subsequently corrected for the instrumental line broadening following S18 (see Equation (5) therein). We produce associated uncertainty maps via error propagation from the estimated noise in the cube. This product creation scheme closely follows S18 and is detailed in A. K. Leroy et al. (2020b, in preparation).

Our masking scheme guarantees high signal-to-noise ratio (S/N) CO line measurements at the expense of excluding faint CO emission, especially from sightlines with low $I_{\rm CO}$ and high $\sigma_{\rm CO}$. The resultant data censoring function is shown in Figure 1 (see formulae in Appendix C). We report in Table A1 (column 12) the CO flux completeness for each galaxy (the flux within the mask divided by the total flux in the data cube, or $f_{\rm CO}$).

Resampling: We resample the two-dimensional maps of $I_{\rm CO}$, $\sigma_{\rm CO}$, and their uncertainties with hexagonal pixels matching the beam size. This ensures that the resampled measurements are nearly mutually independent. We list the number of independent measurements (sightlines) in each galaxy in Table A1 (column 13).

Conversion to physical quantities: We use $\sigma_{\rm CO}$ as a tracer of the molecular gas velocity dispersion, $\sigma_{\rm mol}$. We derive molecular gas surface density, $\Sigma_{\rm mol}$, via

$$\Sigma_{\rm mol} = \alpha_{\rm CO}\, R_{21}^{-1}\, I_{\rm CO}. \quad (1)$$

Here $R_{21} = 0.65$ is the adopted CO (2–1)-to-CO(1–0) line ratio (Leroy et al. 2013b; den Brok et al. 2020) and $\alpha_{\rm CO}$ is the CO-to-H_2 conversion factor. We adopt a metallicity-dependent $\alpha_{\rm CO}$ (similar to the metallicity-dependent part of the xCOLD-GASS prescription; Accurso et al. 2017):

$$\alpha_{\rm CO} = 4.35\, Z'^{-1.6}\, M_\odot\ {\rm pc}^{-2}({\rm K\ km\ s^{-1}})^{-1}, \quad (2)$$

where Z' refers to the local metallicity in units of the solar value. Following Sun et al. (2020), we estimate Z' based on galaxy global stellar mass and effective radius (see Table A1 for values and data sources), assuming a galaxy global mass–

[29] "Physics at High Angular resolution in Nearby GalaxieS with the Atacama Large Millimeter/submillimeter Array." For more information, see www.phangs.org.

[30] Internal data release v3.4.

[31] For the release that we use, the masks begin with all regions with S/N > 3.5 in three consecutive channels. These masks are then expanded to include all adjacent regions with S/N > 2 in two successive channels. The `Python` realization of this signal identification scheme is available at https://github.com/astrojysun/SpectralCubeTools.

[32] Note that for a Gaussian line profile, $\sigma_{\rm CO}$ equals its dispersion.

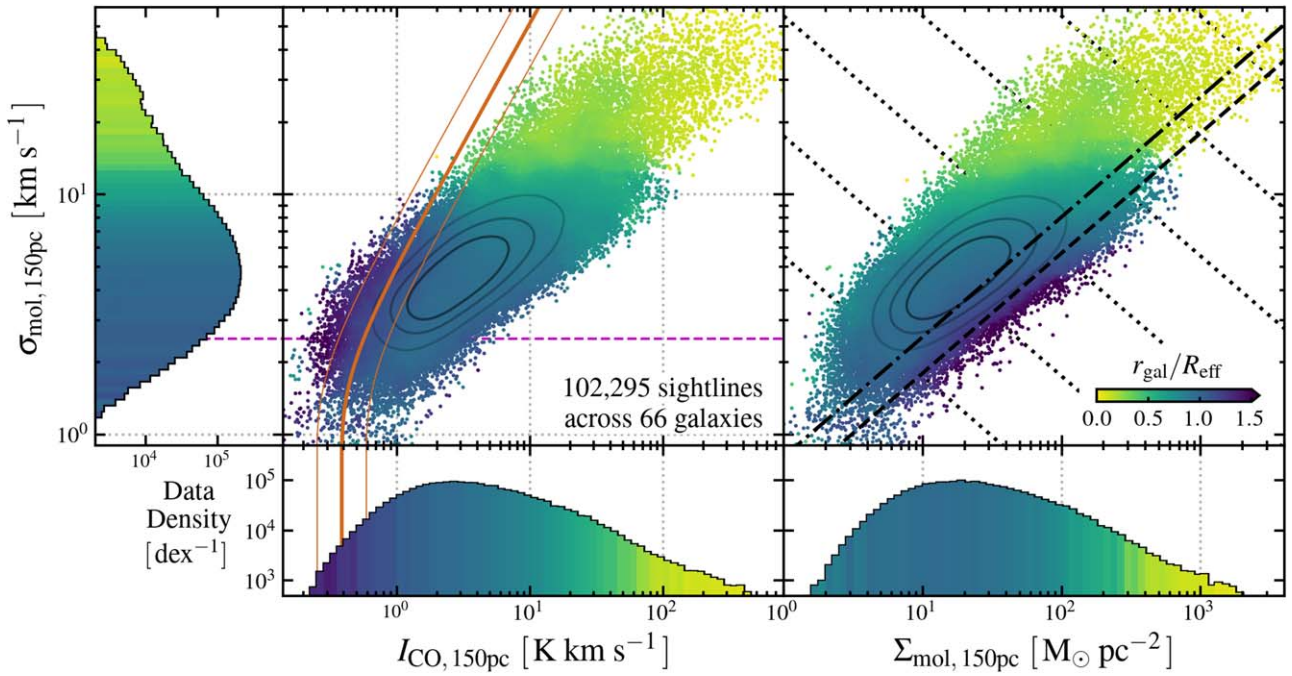

Figure 1. Strong and location-dependent variations in CO line intensity ($I_{\rm CO}$), molecular gas surface density ($\Sigma_{\rm mol}$), and velocity dispersion ($\sigma_{\rm mol}$) on cloud scales in nearby star-forming galaxies. Each of the 102,295 data points represents an independent measurement on a 150 pc scale. Data density contours enclose 30%, 50%, and 70% of data points. Color indicates the galactocentric radius $r_{\rm gal}$ of the measurement normalized by the host galaxy's effective radius $R_{\rm eff}$. Color in the scatter plots represents the median $r_{\rm gal}/R_{\rm eff}$ for data points with similar $I_{\rm CO}$, $\Sigma_{\rm mol}$, and $\sigma_{\rm mol}$. Color in the histograms indicates the median $r_{\rm gal}/R_{\rm eff}$ in each bin. The brown lines show the censoring function, to the left of which little CO emission can be detected. As this function varies from galaxy to galaxy, we use the thick line to show the median and the thin lines to show the 1σ range across all targets. The magenta dashed line indicates the channel width of the CO observations, above which the $\sigma_{\rm mol}$ measurements are most reliable. The black dashed and dashed–dotted lines in the top right panel show the expected relation for beam-filling, spherical GMCs with virial parameter $\alpha_{\rm vir} = 1$ and 2, respectively. The series of dotted lines in the background show the loci of constant $P_{\rm turb}$ (from the lower left to the upper right: $P_{\rm turb} = 10^3$, 10^4,…, $10^8\,k_{\rm B}$ K cm^{-3}).

metallicity relation (Sánchez et al. 2019) and a fixed radial metallicity gradient within a galaxy (Sánchez et al. 2014).

We use $\Sigma_{\rm mol}$ and $\sigma_{\rm mol}$ to estimate the mean turbulent pressure in the molecular gas, $P_{\rm turb} \approx \rho_{\rm mol}\,\sigma^2_{\rm mol}$, and the virial parameter, $\alpha_{\rm vir}$, via

$$P_{\rm turb} = 3.3 \times 10^4\,k_{\rm B}\ {\rm K\ cm^{-3}} \times \left(\frac{\Sigma_{\rm mol}}{10^2\,M_\odot\ {\rm pc^{-2}}}\right)\left(\frac{\sigma_{\rm mol}}{10\ {\rm km\ s^{-1}}}\right)^2\left(\frac{D_{\rm beam}}{150\ {\rm pc}}\right)^{-1}, \quad (3)$$

$$\alpha_{\rm vir} = 3.1 \times \left(\frac{\Sigma_{\rm mol}}{10^2\,M_\odot\ {\rm pc^{-2}}}\right)^{-1}\left(\frac{\sigma_{\rm mol}}{10\ {\rm km\ s^{-1}}}\right)^2\left(\frac{D_{\rm beam}}{150\ {\rm pc}}\right)^{-1}. \quad (4)$$

Here $D_{\rm beam}$ denotes the beam FWHM and is assumed to be the depth along the line of sight.[33] Both equations assume a single, spherical gas structure filling each beam (S18). The second equation assumes in addition that the gas structures have a density profile of $\rho(r) \propto r^{-1}$ (e.g., following Rosolowsky & Leroy 2006).

3. Results

We measure $\Sigma_{\rm mol}$, $\sigma_{\rm mol}$, $P_{\rm turb}$, and $\alpha_{\rm vir}$ on cloud scales in a homogeneous way across our sample. This yields 102,778 independent measurements at 150 pc resolution in 70 galaxies, and 79,840 measurements at 90 pc resolution in 35 galaxies. These measurements are published in Table B1 in machine-readable form. We focus on the 150 pc scale measurements, which are available for all 70 galaxies, while occasionally referencing the 90 pc scale measurements to illustrate resolution dependencies.

In the following data analysis and presentation, we omit measurements from four galaxies (NGC 4207, NGC 4424, NGC 4694, and NGC 4826). These galaxies have edge-on orientation (NGC 4207) and/or peculiar gas kinematics due to ram pressure stripping (NGC 4424), a strong nuclear outflow (NGC 4694), or represent a recent merger event (NGC 4826). We still report results for these galaxies in the tables, but below we focus on the remaining 102,295 sightlines in 66 galaxies for data presentation.

3.1. Statistics of Cloud-scale Molecular Gas Properties

Figure 1 shows the distributions of $I_{\rm CO}$, $\Sigma_{\rm mol}$, and $\sigma_{\rm mol}$, measured at 150 pc resolution. This figure encapsulates molecular gas properties on cloud scales across a wide range of star-forming environments at $z \approx 0$. Table 1 provides area-weighted statistics treating each sightline equally, and $\Sigma_{\rm mol}$-weighted statistics treating each quantum of molecular gas mass equally.

We observe median $I_{\rm CO}$, $\Sigma_{\rm mol}$, and $\sigma_{\rm mol}$ values similar to the results of previous studies (e.g., Bolatto et al. 2008; Colombo et al. 2019), but with a large spread. Across the full sample at 150 pc resolution, we find mass-weighted median $\Sigma_{\rm mol} = 110\,M_\odot$ pc^{-2}

[33] This differs from the assumptions adopted in the complementary cloud identification analysis (E. Rosolowsky et al. 2020, in preparation): in that paper, a gas cloud's extent along the line of sight is limited to <100 pc.

and mass-weighted median $\sigma_{\rm mol} = 9.1$ km s^{-1} (see Table 1). Given the broad sample selection and coverage, these can be taken as typical values across the local star-forming galaxy population. We also see that the $\pm 3\sigma$ (i.e., 99.7%) range of the mass-weighted $\Sigma_{\rm mol}$ and $\sigma_{\rm mol}$ distributions is large, 3.4 and 1.7 dex, respectively. Given that data censoring hinders the detection of low $I_{\rm CO}$ signals (to the left of the brown curves in Figure 1), the true ranges of $I_{\rm CO}$ and $\Sigma_{\rm mol}$ are likely even wider.

We find a strong and statistically significant[34] correlation between $\Sigma_{\rm mol}$ and $\sigma_{\rm mol}$ (Spearman's rank correlation coefficient $\rho = 0.77$). This correlation results in even stronger variations in $P_{\rm turb} \approx \rho_{\rm mol}\, \sigma^2_{\rm mol}$ than those in $\Sigma_{\rm mol}$ or $\sigma_{\rm mol}$ alone. Indeed, $P_{\rm turb}$ varies by $\gtrsim$6 dex at $\pm 3\sigma$ across our sample (Figure 1 and Table 1).

We further compare the observed $\Sigma_{\rm mol} - \sigma_{\rm mol}$ distribution to the expected relations for beam-filling, spherical clouds with fixed virial parameters $\alpha_{\rm vir}$ (black diagonal lines in Figure 1; see Equation (4)). These relations capture the overall trend in the data, with the $\alpha_{\rm vir} = 1$ line lying near their lower envelope. Across our full sample, $\alpha_{\rm vir}$ has a mass-weighted median value of 2.7 and a 1σ scatter of 0.7 dex (Table 1). This means that the kinetic energy in the molecular gas on average slightly exceeds its gravitational binding energy by a factor of 1.3 on 150 pc scales. This is consistent with the conclusion in Sun et al. (2020) that the observed molecular gas velocity dispersion at $\sim$100 pc scales mainly reflects gas motions due to self-gravity and, to a lesser degree, to external gravity and ambient pressure.

The calculation of $P_{\rm turb}$ and $\alpha_{\rm vir}$ assumes an idealized subbeam gas distribution (see Section 2). In reality, the molecular gas remains clumpy on $\lesssim$100 pc spatial scales (Leroy et al. 2013a), and the small-scale density distribution may vary from place to place. These variations in subbeam density distribution may introduce systematic uncertainties in our inferred $P_{\rm turb}$ and $\alpha_{\rm vir}$ values. Nevertheless, our $\Sigma_{\rm mol}$ and $\sigma_{\rm mol}$ measurements should still capture the true distribution of molecular gas properties at the fixed 150 pc spatial scale.

To further illustrate the effect of resolution on our analysis, we compare our measurements at 150 pc scales with those at 90 pc scales for the 32 galaxies that have data at both resolutions (see Table 1 for the statistics at 90 pc). This includes 79,156 independent sightlines at 90 pc scales or 40,641 sightlines at 150 pc scales. We find the mass-weighted medians of $I_{\rm CO}$, $\Sigma_{\rm mol}$, and $P_{\rm turb}$ at 90 pc scales to be moderately higher than the 150 pc scale values by factors of 1.5, 1.5, and 2.0, respectively. However, we see little difference in the median values of $\sigma_{\rm mol}$ and $\alpha_{\rm vir}$ at the two resolutions, and the observed dynamic ranges of all quantities is essentially the same at both spatial scales. This suggests that the gas is moderately clumped below our resolution, but that our qualitative conclusions are not sensitive to resolution-related biases and robustly reflect typical molecular gas properties at $\sim$100 pc scales.

3.2. Correlation with Galactocentric Radius

The variations in $I_{\rm CO}$, $\Sigma_{\rm mol}$, and $\sigma_{\rm mol}$ correlate with location in the host galaxy. To illustrate this, we color-code all data points in Figure 1 by their galactocentric radii ($r_{\rm gal}$), normalized to the effective radii of their host galaxies ($R_{\rm eff}$; see Table A1 for values and data sources). Both $\Sigma_{\rm mol}$ and $\sigma_{\rm mol}$ tend to increase toward smaller $r_{\rm gal}/R_{\rm eff}$. Additionally, the gas in the inner regions ($r_{\rm gal}/R_{\rm eff} < 0.5$) frequently shows enhanced $\sigma_{\rm mol}$ at a given $\Sigma_{\rm mol}$.

These radial trends are partly driven by the structure of galaxy disks. Most star-forming galaxies show increasing gas and stellar mass surface densities toward their central regions. This leads to a similar radial trend on the mean pressure in the interstellar medium (ISM) required to keep it in vertical dynamical equilibrium (Elmegreen 1989; Blitz & Rosolowsky 2004; Ostriker et al. 2010). We expect the same trend to hold for the turbulent pressure in the molecular gas, $P_{\rm turb}$, which correlates with the mean ISM pressure (Sun et al. 2020). This expectation matches well with the trend of decreasing $r_{\rm gal}/R_{\rm eff}$ with increasing $P_{\rm turb}$ values in Figure 1.

The expectation from ISM dynamical equilibrium does not by itself explain all the trends in Figure 1—for fixed $\Sigma_{\rm mol}$, we also find excess $\sigma_{\rm mol}$ at smaller $r_{\rm gal}/R_{\rm eff}$. At face value, this suggests that molecular gas in the inner galaxy tends to be more weakly bound (higher $\alpha_{\rm vir}$) than the gas in the outer galaxy. Such a trend is expected from the larger contribution of the external (mostly stellar) potential to the dynamical equilibrium at smaller radii (e.g., S18; Meidt et al. 2018; Gensior et al. 2020). However, the observed trend could instead suggest that the gas is more clumpy in the inner parts of galaxies, or that our prescription overpredicts $\alpha_{\rm CO}$ in the outer disks of galaxies. If we adopt an alternative prescription with $\alpha_{\rm CO} \propto Z'^{-0.5}$ (as suggested by recent numerical simulations; M. Gong et al., private communication), the apparent trend of lower $\sigma_{\rm mol}$ at fixed $\Sigma_{\rm mol}$ toward the outer disks (i.e., $r_{\rm gal}/R_{\rm eff} \gtrsim 1.5$) would disappear. But the elevated $\sigma_{\rm mol}$ at fixed $\Sigma_{\rm mol}$ near the galaxy centers (i.e., $r_{\rm gal}/R_{\rm eff} \lesssim 0.5$) would persist and thus cannot be explained by $\alpha_{\rm CO}$ alone.

The trend with galactocentric radius at fixed $\Sigma_{\rm mol}$ may also reflect biases in the line width measurement. Using the CO rotation curves from Lang et al. (2020), we verified that unresolved rotation often represents a minor contribution to our measured line width at 90–150 pc scales in the inner parts of galaxies. However, unresolved noncircular motions may still play an important role (e.g., Colombo et al. 2014b; Meidt et al. 2018, 2020; Henshaw et al. 2020).

3.3. Correlation with Galaxy Bars and Spiral Arms

We investigate whether galaxy morphological features, i.e., stellar bars and spiral arms, have an impact on the molecular gas properties on cloud scales. We classify each target galaxy as barred or unbarred (see Table A1), and divide the PHANGS–ALMA CO footprint into a central region and a disk region based on near-infrared images. The central regions often correspond to distinct structures (e.g., nuclear rings) showing extra light at near-infrared wavelengths. For galaxies with strong spiral arms, we further identify arm regions and the corresponding inter-arm regions covering the same $r_{\rm gal}$ range. The methodology closely follows Salo et al. (2015) and Herrera-Endoqui et al. (2015) and is detailed in M. Querejeta et al. (2020, in preparation).

The left panel of Figure 2 compares molecular gas properties in the central regions and the disk regions of our galaxies. Motivated by previous studies (e.g., Sakamoto et al. 1999; Jogee et al. 2005, S18), we indicate the centers of 43 galaxies

[34] Here and in subsequent sections "statistically significant" means p – value $\ll 0.001$.

classified as barred and 13 galaxies classified as unbarred separately.[35] The centers of barred galaxies show ∼20 times higher mass-weighted median $\Sigma_{\rm mol}$ and ∼5 times higher mass-weighted median $\sigma_{\rm mol}$ compared to the disk regions (Table 1). These central regions of barred galaxies mostly host molecular gas with $\Sigma_{\rm mol} \gtrsim 100\,M_\odot\,{\rm pc}^{-2}$ and $\sigma_{\rm mol} \gtrsim 10\,{\rm km\,s}^{-1}$ and commonly show excess in star formation. A small fraction of the gas in the centers of unbarred galaxies also shows high $\Sigma_{\rm mol}$ and $\sigma_{\rm mol}$, but the majority resembles the gas in the disk regions. This sharp contrast between barred and unbarred galaxies indicates that the high $\Sigma_{\rm mol}$ and $\sigma_{\rm mol}$ frequently found in star-forming galaxy centers is linked to the presence of stellar bars.

Our measurements in galaxy centers can be affected by uncertainty related to $\alpha_{\rm CO}$ and R_{21}. Sandstrom et al. (2013) and den Brok et al. (2020) find evidence for low $\alpha_{\rm CO}$ and high R_{21} in star-forming galaxy centers. If our prescription also accounted for these effects, the $\Sigma_{\rm mol}$ enhancement would be reduced in galaxy centers, but the excess in $\sigma_{\rm mol}$ at a given $\Sigma_{\rm mol}$ would be even more extreme relative to disks.

The observed extreme gas properties in barred galaxy centers are consistent with existing knowledge about the role of stellar bars in regulating ISM properties. Stellar bars can drive large-scale gas inflows, boosting the central gas reservoir and leading to high $\Sigma_{\rm mol}$ (e.g., Pfenniger & Norman 1990; Sakamoto et al. 1999; Sheth et al. 2002; Jogee et al. 2005; Tress et al. 2020b). Meanwhile, the released gravitational energy from gas inflow as well as the stronger local stellar and AGN feedback together enhance the local turbulence (e.g., Kruijssen et al. 2014; Armillotta et al. 2019; Sormani et al. 2019). Complex gas streaming motions that are unresolved in our data could also bias $\sigma_{\rm mol}$ higher than the turbulent velocity dispersion (e.g., Henshaw et al. 2016).

The right panel in Figure 2 compares the distribution of $\Sigma_{\rm mol}$ at fixed $r_{\rm gal}/R_{\rm eff}$ in spiral arm regions and inter-arm regions for 28 galaxies with identifiable spiral structures in their stellar distribution. Molecular gas in the arm regions shows typically 1.5–2 times higher $\Sigma_{\rm mol}$ relative to the gas in the inter-arm regions at fixed $r_{\rm gal}/R_{\rm eff}$. We further find (not shown in Figure 2) that the gas in spiral arms shows ∼20% higher $\sigma_{\rm mol}$, ∼2–3 times higher $P_{\rm turb}$, and ∼15% lower $\alpha_{\rm vir}$ at fixed $r_{\rm gal}/R_{\rm eff}$. Consistent with previous studies examining individual galaxies (e.g., Hughes et al. 2013b; Colombo et al. 2014a; Hirota et al. 2018), these results support the idea that spiral arms harbor more high surface density, turbulent, bound molecular clouds.

Though statistically significant, the measured contrast in $\Sigma_{\rm mol}$ between arms and inter-arm gas may seem lower than what one would expect from visual inspection of the PHANGS–ALMA CO maps (e.g., Figure 12 in S18). There the spiral arms typically appear replete with bright emission, while the inter-arm regions show only a sporadic, faint signal with a large portion of the area lacking significant CO detection. We note that our quantitative analysis focuses solely on the gas securely detected in CO without accounting for the area covering fraction of the CO detection. Had we included map pixels with non- or low-significance detections in our analysis, measurements in the inter-arm regions would be more severely diluted than measurements in the arm regions, and the arm versus inter-arm contrast would be considerably larger than the factor of 1.5–2 measured above (also see M. Querejeta et al. 2020, in preparation).

[35] The remaining 10 galaxies have ambiguous classifications (see Table A1). Measurements in their central regions are omitted in Figure 2.

To summarize, our measurements based on significant detections of CO emission reveal moderate differences between the molecular gas properties in spiral arm versus inter-arm regions. In addition to this, the spatial density of secure CO detections is much lower in the inter-arm regions than in the spiral arms of galaxies. Together, these two observations suggest that spiral arms not only accumulate molecular gas but also lightly modify the properties of the gas (e.g., Dobbs & Bonnell 2008; Tress et al. 2020a).

3.4. Correlation with Integrated Galaxy Properties

We find that molecular gas properties on cloud scales correlate with integrated properties of the host galaxies. In Figure 3, the top left panel shows the mass-weighted median $\Sigma_{\rm mol}$ and $\sigma_{\rm mol}$ values on 150 pc scale within each galaxy, with each point colored by the galaxy global star formation rate (SFR). The top right panel shows how the galaxy-wide, mass-weighted median $\Sigma_{\rm mol}$ varies among galaxies across the galaxy global $M_\star$ − SFR space.

Across our sample, the mass-weighted median $\Sigma_{\rm mol}$ and $\sigma_{\rm mol}$ vary by 2 dex and 1 dex from galaxy to galaxy, respectively. These cloud-scale gas properties also show statistically significant correlations with host galaxy global $M_\star$ (Spearman's $\rho = 0.64$ and 0.53), global SFR ($\rho = 0.72$ and 0.58), and offset in SFR from the local star-forming main sequence (ΔMS; $\rho = 0.45$ and 0.35). We also find positive correlations between the mass-weighted median $P_{\rm turb}$ and the same galaxy global properties (not shown in Figure 3). The mass-weighted median of $\alpha_{\rm vir}$, however, shows an anticorrelation with the galaxy's SFR ($\rho = -0.44$) and ΔMS ($\rho = -0.41$). Figure 3 only shows the 150 pc results, but we see similar trends using data at 90 pc resolution.

The pronounced galaxy-to-galaxy variations in these mass-weighted median quantities is partly explained by galaxies in our sample that host a distinct central concentration of CO-bright molecular gas. This is especially true of barred galaxies, where the central regions host a substantial fraction of the galaxy's molecular gas mass. In these galaxies, the exceptional gas properties in the central region bias the galaxy-wide mass-weighted median measurements toward high $\Sigma_{\rm mol}$ and $\sigma_{\rm mol}$. In light of this bias, we also calculate and compare the mass-weighted median properties for all the CO emission *outside* the central region in each galaxy. As shown in the bottom panels in Figure 3, excluding the central regions reduces the level of galaxy-to-galaxy variations in the mass-weighted median $\Sigma_{\rm mol}$ and $\sigma_{\rm mol}$. Nevertheless, the overall trends persist, and the rank correlation of the median $\Sigma_{\rm mol}$, $\sigma_{\rm mol}$, and $P_{\rm turb}$ with all three global galaxy properties remain significant.

Across the local star-forming galaxy population, we thus conclude that the molecular gas in more massive and actively star-forming galaxies is systematically denser (as traced by $\Sigma_{\rm mol}$), more turbulent (as tracked by $\sigma_{\rm mol}$ and $P_{\rm turb}$), and more strongly self-gravitating (as expressed by $\alpha_{\rm vir}$) on ∼100 pc scales. We speculate that these trends arise because galaxy global properties correlate with the structural properties on a more *local* scale (e.g., local stellar mass distribution, galaxy dynamical features). In turn, molecular gas properties on cloud scales are linked to these local structural properties (e.g., Hughes et al. 2013a; Meidt et al. 2018, 2020; Schruba et al. 2019; Chevance et al. 2020; Sun et al. 2020). We plan to investigate this topic in more detail in a future round of PHANGS–ALMA analysis.

Table 1
Statistics of Cloud-scale Molecular Gas Properties

Quantity	Unit	Area-weighted			Mass-weighted		
		Median	1σ Range (68.3%)	3σ Range (99.7%)	Median	1σ Range (68.3%)	3σ Range (99.7%)
Full Sample at 150 pc Scales (102,295 Sightlines across 66 Galaxies; See Section 3.1)							
$I_{\rm CO,150pc}$	K km s^{-1}	3.4×10^{0}	0.9 dex	3.2 dex	1.9×10^{1}	1.6 dex	3.6 dex
$\Sigma_{\rm mol,150pc}$	$M_\odot$ pc^{-2}	2.2×10^{1}	0.9 dex	2.9 dex	1.1×10^{2}	1.5 dex	3.4 dex
$\sigma_{\rm mol,150pc}$	km s^{-1}	5.0×10^{0}	0.4 dex	1.7 dex	9.1×10^{0}	0.8 dex	1.7 dex
$P_{\rm turb,150pc}$	$k_{\rm B}$ K cm^{-3}	1.8×10^{4}	1.6 dex	6.1 dex	3.0×10^{5}	3.0 dex	6.5 dex
$\alpha_{\rm vir,150pc}$	⋯	3.5	0.6 dex	1.9 dex	2.7	0.7 dex	2.0 dex
Gas in Galaxy Disks at 150 pc Scales (99,765 Sightlines across 66 Galaxies; See Sections 3.3 and 3.4)							
$I_{\rm CO,150pc}$	K km s^{-1}	3.3×10^{0}	0.9 dex	2.7 dex	1.2×10^{1}	1.1 dex	3.0 dex
$\Sigma_{\rm mol,150pc}$	$M_\odot$ pc^{-2}	2.1×10^{1}	0.9 dex	2.5 dex	7.1×10^{1}	1.0 dex	2.8 dex
$\sigma_{\rm mol,150pc}$	km s^{-1}	4.9×10^{0}	0.4 dex	1.6 dex	7.5×10^{0}	0.5 dex	1.6 dex
$P_{\rm turb,150pc}$	$k_{\rm B}$ K cm^{-3}	1.7×10^{4}	1.6 dex	5.4 dex	1.3×10^{5}	1.9 dex	5.6 dex
$\alpha_{\rm vir,150pc}$	⋯	3.4	0.6 dex	1.9 dex	2.7	0.7 dex	2.0 dex
Gas in the Centers of Barred Galaxies at 150 pc Scales (1,715 Sightlines across 43 Galaxies; See Section 3.3)							
$I_{\rm CO,150pc}$	K km s^{-1}	6.5×10^{1}	1.3 dex	3.4 dex	3.0×10^{2}	0.9 dex	2.6 dex
$\Sigma_{\rm mol,150pc}$	$M_\odot$ pc^{-2}	2.8×10^{2}	1.3 dex	3.4 dex	1.3×10^{3}	0.9 dex	2.6 dex
$\sigma_{\rm mol,150pc}$	km s^{-1}	2.3×10^{1}	0.5 dex	1.7 dex	3.4×10^{1}	0.4 dex	1.2 dex
$P_{\rm turb,150pc}$	$k_{\rm B}$ K cm^{-3}	5.1×10^{6}	2.1 dex	6.5 dex	5.0×10^{7}	1.3 dex	4.3 dex
$\alpha_{\rm vir,150pc}$	⋯	6.0	0.8 dex	2.1 dex	2.7	0.7 dex	2.1 dex
Full Sample at 90 pc Scales (79,156 Sightlines across 32 Galaxies; See Section 3.1)							
$I_{\rm CO,90pc}$	K km s^{-1}	4.2×10^{0}	0.9 dex	2.9 dex	1.5×10^{1}	1.2 dex	3.3 dex
$\Sigma_{\rm mol,90pc}$	$M_\odot$ pc^{-2}	2.6×10^{1}	0.8 dex	2.6 dex	8.7×10^{1}	1.1 dex	3.1 dex
$\sigma_{\rm mol,90pc}$	km s^{-1}	4.5×10^{0}	0.4 dex	1.6 dex	7.0×10^{0}	0.6 dex	1.7 dex
$P_{\rm turb,90pc}$	$k_{\rm B}$ K cm^{-3}	2.9×10^{4}	1.5 dex	5.5 dex	2.3×10^{5}	2.2 dex	6.3 dex
$\alpha_{\rm vir,90pc}$	⋯	3.8	0.6 dex	1.8 dex	3.1	0.6 dex	1.8 dex
Gas in Galaxy Disks at 90 pc Scales (76,500 Sightlines across 32 Galaxies)							
$I_{\rm CO,90pc}$	K km s^{-1}	4.1×10^{0}	0.8 dex	2.6 dex	1.2×10^{1}	1.0 dex	2.8 dex
$\Sigma_{\rm mol,90pc}$	$M_\odot$ pc^{-2}	2.6×10^{1}	0.8 dex	2.4 dex	7.1×10^{1}	1.0 dex	2.6 dex
$\sigma_{\rm mol,90pc}$	km s^{-1}	4.4×10^{0}	0.4 dex	1.5 dex	6.3×10^{0}	0.4 dex	1.4 dex
$P_{\rm turb,90pc}$	$k_{\rm B}$ K cm^{-3}	2.7×10^{4}	1.5 dex	5.0 dex	1.6×10^{5}	1.8 dex	5.0 dex
$\alpha_{\rm vir,90pc}$	⋯	3.7	0.6 dex	1.8 dex	2.9	0.6 dex	1.8 dex

Note. The area-weighted statistics are derived from percentiles weighted by sightline number counts, whereas the mass-weighted statistics from percentiles weighted by molecular gas mass (equivalent to $\Sigma_{\rm mol}$ in our measurement scheme).

4. Summary

Using the full PHANGS–ALMA CO (2–1) data set, we measure molecular gas surface density, velocity dispersion, turbulent pressure, and virial parameter on cloud scales in 70 nearby, massive, star-forming galaxies. We publish the resultant 102,778 independent measurements at 150 pc scales and 79,840 measurements at 90 pc scales in Table B1 and summarize their statistics in Table 1 and Section 3.1.

Consistent with observations in the PHANGS–ALMA pilot sample (S18) and other galaxies (e.g., Hughes et al. 2013b; Egusa et al. 2018), we find that molecular gas properties on $\sim$100 pc scales vary substantially and correlate with location in the host galaxy. Specifically, our key results are:

1. Molecular gas surface density, velocity dispersion, and turbulent pressure vary dramatically (by 3.4, 1.7, and 6.5 dex, respectively) across our full sample. The correlation between surface density and velocity dispersion suggests that the gas motions on $\sim$100 pc scales are mainly responding to gas self-gravity, though they do also react to external gravity and/or ambient pressure in some regions. The inferred virial parameter has a median value of 2.7 and a 1σ range of 0.7 dex (Figure 1 and Section 3.1).
2. The cloud-scale gas surface density, velocity dispersion, and turbulent pressure all increase toward small galactocentric radii, consistent with expectations from vertical dynamical equilibrium and the structure of galaxy disks (Figure 1 and Section 3.2).
3. The centers of barred galaxies display exceptionally high molecular gas surface densities and velocity dispersions. The high surface densities are likely fueled by gas inflows induced by the stellar bars. The observed excess velocity dispersion at fixed surface density in these regions suggests less bound gas or enhanced bulk flow motions (Figure 2 and Section 3.3).
4. Molecular gas in spiral arm regions shows moderately higher surface densities and appears more turbulent and more bound than the molecular gas detected in the interarm regions. This suggests that spiral arms accumulate

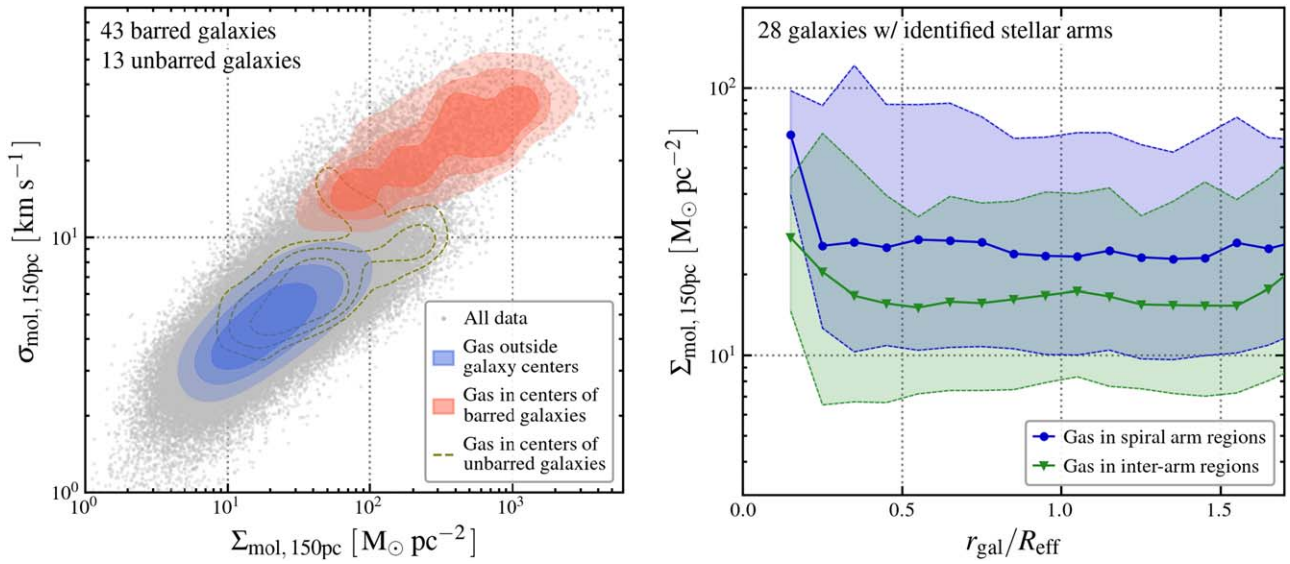

Figure 2. Left: molecular gas in the centers of barred galaxies shows distinctively high $\Sigma_{\rm mol}$ and $\sigma_{\rm mol}$. Data density contours show the distribution of measurements in galaxy disks (i.e., outside the central regions; blue filled contours), in the centers of 43 identified barred galaxies (red filled contours), and in the centers of 13 unbarred galaxies (brown dashed contours). We see typical gas properties of $\Sigma_{\rm mol} \gtrsim 100\,M_\odot$ pc^{-2} and $\sigma_{\rm mol} \gtrsim 10$ km s^{-1} in the centers of barred galaxies. This is in sharp contrast to the gas properties in galaxy disks and in the centers of unbarred galaxies. Right: molecular gas in spiral arms displays higher $\Sigma_{\rm mol}$ than the gas in inter-arm regions at given galactocentric radii. The blue and green curves show the trends of median $\Sigma_{\rm mol}$ in each $r_{\rm gal}/R_{\rm eff}$ bin for the gas in spiral arms and inter-arm regions, respectively. Shaded regions denote the 1σ (68.3%) range of the binned data distribution. In the 28 galaxies exhibiting stellar spiral structures, the gas in the spiral arms typically shows 1.5–2 times higher $\Sigma_{\rm mol}$ than the detected gas in the inter-arm regions at the same $r_{\rm gal}/R_{\rm eff}$.

molecular gas and further mildly alter the gas properties (Figure 2 and Section 3.3).

5. The properties of molecular gas at cloud-scale resolution correlate with the properties of the host galaxy. Galaxies with higher stellar mass and more active star formation tend to host molecular gas with higher surface density, higher velocity dispersion, and lower virial parameter (Figure 2 and Section 3.4).

These observations provide a first comprehensive view of the the properties of molecular gas at cloud scales across the local star-forming galaxy population. They provide strong evidence that molecular cloud properties are closely coupled to the galactic environment, likely through dynamical processes and stellar feedback. The empirical relations presented in this work establish the groundwork for unveiling the physics that underpins the molecular cloud–environment connection.

This work was carried out as part of the PHANGS collaboration. The work of J.S., A.K.L., and D.U. is partially supported by the National Science Foundation (NSF) under grant Nos. 1615105, 1615109, and 1653300, as well as by the National Aeronautics and Space Administration (NASA) under ADAP grants NNX16AF48G and NNX17AF39G. E.S., D.L., T.S., and T.G.W. acknowledge funding from the European Research Council (ERC) under the European Unions Horizon 2020 research and innovation program (grant agreement No. 694343). E.R. acknowledges the support of the Natural Sciences and Engineering Research Council of Canada (NSERC), funding reference number RGPIN-2017-03987. A. U. acknowledges support from the Spanish funding grants AYA2016-79006-P (MINECO/FEDER) and PGC2018-094671-B-I00 (MCIU/AEI/FEDER). J.M.D.K., M.C, and J.J.K. gratefully acknowledge funding from the DFG through an Emmy Noether Research Group (grant No. KR4801/1-1) and the DFG Sachbeihilfe (grant No. KR4801/2-1). J.M.D.K. gratefully acknowledges funding from the European Research Council (ERC) under the European Union's Horizon 2020 research and innovation program via the ERC Starting Grant MUSTANG (grant agreement No. 714907). F.B. acknowledges funding from the European Unions Horizon 2020 research and innovation program (grant agreement No. 726384/EMPIRE). R.S.K. and S.C.O.G. acknowledge financial support from the German Research Foundation (DFG) via the collaborative research center (SFB 881, Project-ID 138713538) "The Milky Way System" (subprojects A1, B1, B2, and B8). They also acknowledge funding from the Heidelberg Cluster of Excellence STRUCTURES in the framework of Germany's Excellence Strategy (grant EXC-2181/1 - 390900948) and from the European Research Council via the ERC Synergy Grant ECOGAL (grant 855130) and the ERC Advanced Grant STARLIGHT (grant 339177). K.K. gratefully acknowledges funding from the Deutsche Forschungsgemeinschaft (DFG, German Research Foundation) in the form of an Emmy Noether Research Group (grant No. KR4598/2-1, PI: Kreckel). A.E.S. is supported by an NSF Astronomy and Astrophysics Postdoctoral Fellowship under award AST-1903834.

This Letter makes use of the following ALMA data: ADS/JAO.ALMA#2012.1.00650.S, ADS/JAO.ALMA#2013.1.01161.S, ADS/JAO.ALMA#2015.1.00925.S, ADS/JAO.ALMA#2015.1.00956.S, ADS/JAO.ALMA#2017.1.00392.S, ADS/JAO.ALMA#2017.1.00886.L, ADS/JAO.ALMA#2018.1.01321.S, ADS/JAO.ALMA#2018.1.01651.S. ALMA is a partnership of ESO (representing its member states), NSF (USA), and NINS (Japan), together with NRC (Canada), NSC and ASIAA (Taiwan), and KASI (Republic of Korea), in cooperation with the Republic of Chile. The Joint ALMA Observatory is operated by ESO, AUI/NRAO, and NAOJ. The National Radio Astronomy Observatory is a facility of the National Science Foundation operated under cooperative agreement by Associated Universities, Inc.

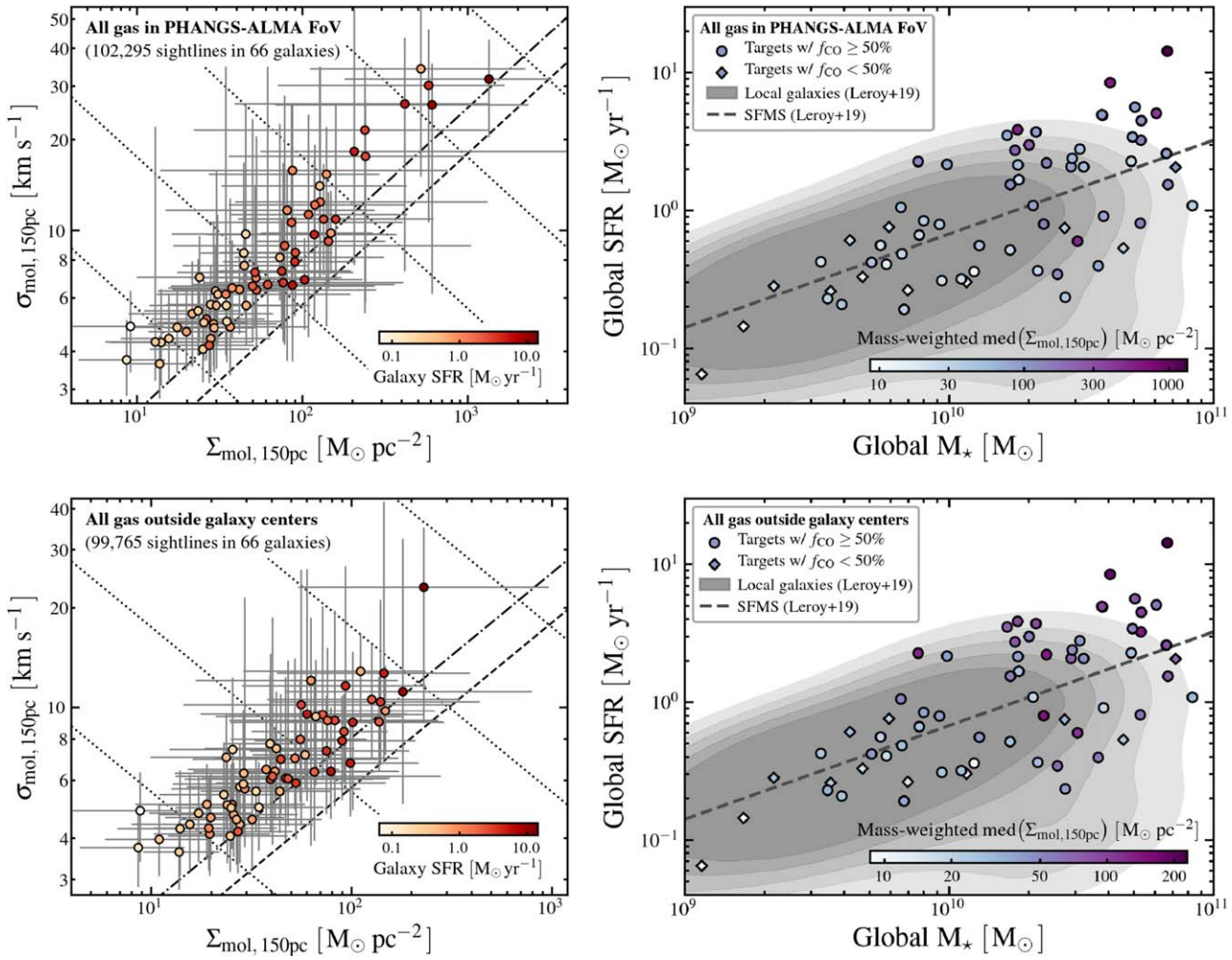

Figure 3. Molecular gas in more massive and more actively star-forming galaxies shows higher surface densities $\Sigma_{\rm mol}$ and velocity dispersions $\sigma_{\rm mol}$ on 150 pc scales. Top left: each point shows the mass-weighted median value of $\Sigma_{\rm mol}$ and $\sigma_{\rm mol}$ across the PHANGS–ALMA field of view in a galaxy, and the error bars indicate their 1σ (68.3%) range. The diagonal lines represent constant loci of $\alpha_{\rm vir}$ and $P_{\rm turb}$ as in Figure 1. Galaxies with a higher global SFR (denoted by darker color) tend to show higher median $\Sigma_{\rm mol}$ and $\sigma_{\rm mol}$ on cloud scales. Top right: the 66 galaxies studied here (large symbols) are color-coded by their galaxy-wide, gas mass-weighted median $\Sigma_{\rm mol}$ and overlaid on the $M_\star$ – SFR distribution of all local galaxies (gray contours; Leroy et al. 2019). Galaxies with low (<50%) CO flux completeness are shown with a different symbol. The disk-wide median $\Sigma_{\rm mol}$ shows significant correlation with galaxy global properties, including stellar mass, SFR, and offset from the star-forming main sequence (gray dashed line; Leroy et al. 2019). Bottom panels: similar to the top panels, but with each point showing the statistics for all the gas outside the central regions in each galaxy. The galaxy-to-galaxy variations in gas properties become smaller, but the same general trends with galaxy global properties persist. The single outlier showing high mass-weighted median $\sigma_{\rm mol}$ in the bottom left panel is NGC 1365, for which the PHANGS–ALMA CO map only covers the stellar bar-covered inner part of the galaxy.

We acknowledge the usage of the Extragalactic Distance Database (http://edd.ifa.hawaii.edu/index.html; Tully et al. 2009) and the SAO/NASA Astrophysics Data System (http://www.adsabs.harvard.edu).

Facility: ALMA.

Software: `CASA` (McMullin et al. 2007), `Astropy` (Astropy Collaboration et al. 2018), `spectral-cube` (Ginsburg et al. 2019), `SpectralCubeTools` (https://github.com/astrojysun/SpectralCubeTools).

Appendix A
Galaxy Sample

We list our galaxy sample in Table A1.

Table A1
Galaxy Sample

Galaxy	Bar	Arm	d (Mpc)	i (deg)	θ_{PA} (deg)	$M_\star$ ($10^9\,M_\odot$)	SFR ($M_\odot\,yr^{-1}$)	R_{eff} (kpc)	$T_{noise,\,150pc}$ (K)	$r_{ch,\,150pc}$	$f_{CO,\,150pc}$	$N_{los,\,150pc}$
(1)	(2)	(3)	(4)	(5)	(6)	(7)	(8)	(9)	(10)	(11)	(12)	(13)
Circinus[a]	?	N	4.21	64.3	36.7	18.2	3.85	2.5	0.048	0.072	83%	456
IC 1954	Y	Y	15.2	57.2	63.7	6.6	0.48	3.0	0.026	0.059	79%	1054
IC 5273	Y	N	14.7	48.5	235.2	5.5	0.56	2.3	0.022	0.055	64%	750
NGC 253[a]	Y	N	3.68	75.0	52.5	38.0	4.90	4.4	0.031	0.072	88%	2203
NGC 300[a]	N	N	2.08	39.8	11.4	1.7	0.14	2.2	0.011	0.123	41%	127
NGC 628	N	Y	9.77	8.7	20.8	18.3	1.67	4.6	0.031	0.061	83%	3239
NGC 685	Y	N	16.0	32.7	99.9	7.0	0.26	4.0	0.029	0.058	41%	615
NGC 1087	Y	N	14.4	40.5	357.4	6.6	1.05	3.0	0.040	0.055	75%	1165
NGC 1097	Y	Y	14.2	48.6	122.8	60.8	5.08	5.4	0.032	0.062	85%	3093
NGC 1300	Y	Y	26.1	31.8	276.9	71.9	2.06	9.1	0.096	0.054	48%	1037
NGC 1317	Y	N	19.0	24.5	221.5	36.6	0.40	4.4	0.032	0.063	105%[c]	575
NGC 1365	Y	Y	18.1	55.4	202.4	66.8	14.34	11.8	0.067	0.191	88%	2073
NGC 1385	?	Y	22.7	45.4	179.6	16.6	3.50	4.9	0.072	0.054	67%	1796
NGC 1433	Y	N	16.8	28.6	198.0	52.9	0.81	8.3	0.057	0.055	58%	684
NGC 1511	?	N	15.6	73.5	296.9	7.6	2.27	2.8	0.038	0.063	89%	778
NGC 1512	Y	Y	16.8	42.5	263.8	38.3	0.91	7.2	0.052	0.057	61%	689
NGC 1546	N	N	18.0	70.1	147.8	22.8	0.80	3.2	0.030	0.057	97%	972
NGC 1559	Y	N	19.8	58.7	245.9	21.3	3.72	3.5	0.056	0.056	75%	2218
NGC 1566	Y	Y	18.0	30.5	216.5	53.3	4.49	8.4	0.057	0.058	97%	3944
NGC 1637	Y	Y	9.77	31.1	20.6	7.7	0.66	1.1	0.012	0.054	91%	1360
NGC 1672	Y	Y	11.9	43.8	135.9	17.7	2.73	5.1	0.052	0.064	82%	1291
NGC 1792	N	N	12.8	64.7	318.9	23.3	2.21	3.2	0.028	0.066	94%	1468
NGC 2090	N	Y	11.8	64.4	192.4	11.1	0.32	2.5	0.042	0.061	80%	516
NGC 2283	Y	Y	10.4	44.2	356.2	3.6	0.26	2.1	0.036	0.061	44%	287
NGC 2566	Y	Y	23.7	48.5	312.0	40.6	8.47	5.7	0.072	0.064	79%	1978
NGC 2835	Y	Y	10.1	41.1	0.2	5.9	0.76	2.8	0.056	0.060	28%	182
NGC 2903	Y	N	8.47	67.0	205.4	28.9	2.08	4.5	0.026	0.065	90%	2390
NGC 2997	?	Y	11.3	31.9	109.3	31.2	2.79	5.0	0.026	0.063	86%	5380
NGC 3137	?	N	14.9	70.1	358.9	5.8	0.41	4.6	0.033	0.056	70%	488
NGC 3351	Y	N	10.0	45.1	193.2	20.8	1.09	3.1	0.039	0.062	74%	991
NGC 3507	Y	Y	20.9	24.2	55.6	27.3	0.75	3.5	0.067	0.060	45%	1090
NGC 3511	Y	N	9.95	75.0	256.7	5.1	0.42	3.0	0.020	0.058	87%	769
NGC 3521	N	N	11.2	69.0	343.0	66.3	2.59	5.6	0.023	0.056	90%	3770
NGC 3596	N	N	10.1	21.6	78.1	3.5	0.23	1.7	0.052	0.060	72%	495
NGC 3621	N	N	6.56	65.4	343.8	9.2	0.79	2.9	0.013	0.063	91%	1487
NGC 3626	Y	N	20.0	46.6	165.2	27.5	0.23	3.3	0.084	0.057	57%	150
NGC 3627	Y	Y	10.57	56.5	174.0	53.1	3.24	5.2	0.033	0.061	89%	2933
NGC 4207[b]	?	N	16.8	62.5	120.5	5.1	0.22	1.3	0.062	0.067	91%	147
NGC 4254	N	Y	16.8	35.3	68.5	37.8	4.95	3.6	0.053	0.056	84%	6438
NGC 4293	Y	N	16.0	65.0	48.3	30.6	0.60	3.8	0.061	0.075	81%	164
NGC 4298	N	N	16.8	59.6	314.1	13.0	0.56	2.7	0.025	0.056	93%	2328
NGC 4303	Y	Y	17.6	20.0	310.6	50.4	5.63	6.2	0.066	0.061	82%	3945
NGC 4321	Y	Y	15.2	39.1	157.7	49.4	3.41	6.2	0.058	0.058	77%	4923
NGC 4424[b]	?	N	16.4	58.2	88.3	8.3	0.31	3.3	0.060	0.071	103%[c]	123
NGC 4457	Y	N	15.6	17.4	78.7	25.7	0.34	3.1	0.041	0.060	93%	645
NGC 4496A	Y	N	14.9	55.3	49.7	4.2	0.61	3.1	0.057	0.058	29%	168
NGC 4535	Y	Y	15.8	42.1	179.3	32.3	2.07	5.8	0.053	0.059	75%	2433
NGC 4536	Y	Y	15.2	64.8	307.4	20.0	2.99	4.2	0.025	0.059	88%	2025
NGC 4540	Y	N	16.8	38.3	14.3	6.8	0.19	1.8	0.059	0.063	65%	428
NGC 4548	Y	Y	16.2	38.3	138.0	45.6	0.53	5.1	0.035	0.060	49%	1027
NGC 4569	Y	N	16.8	70.0	18.0	67.2	1.54	8.9	0.038	0.058	85%	2544
NGC 4571	N	N	14.9	31.9	217.4	11.6	0.30	3.3	0.058	0.059	42%	711
NGC 4579	Y	Y	16.8	37.3	92.5	83.1	1.08	5.7	0.039	0.057	70%	3078
NGC 4689	N	N	16.8	39.0	164.3	17.0	0.52	4.2	0.060	0.058	72%	1827
NGC 4694[b]	N	N	16.8	60.7	143.3	7.8	0.15	3.0	0.055	0.056	38%	76
NGC 4731	Y	Y	12.4	64.0	255.4	3.3	0.42	4.0	0.017	0.052	56%	261
NGC 4781	Y	N	15.3	56.4	288.1	8.0	0.84	2.4	0.022	0.055	79%	1411
NGC 4826[b]	N	N	4.36	58.6	293.9	16.0	0.20	1.7	0.014	0.068	97%	147
NGC 4941	?	N	14.0	53.1	202.6	12.4	0.36	3.4	0.020	0.054	80%	1196
NGC 4951	N	N	12.0	70.5	92.0	3.9	0.21	2.5	0.034	0.063	71%	214
NGC 5042	?	N	12.6	51.4	190.1	4.7	0.33	2.9	0.035	0.056	35%	300
NGC 5068	Y	N	5.16	27.0	349.0	2.2	0.28	2.1	0.037	0.065	46%	222

Table A1
(Continued)

Galaxy	Bar	Arm	d (Mpc)	i (deg)	θ_{PA} (deg)	$M_\star$ ($10^9\,M_\odot$)	SFR ($M_\odot\,yr^{-1}$)	R_{eff} (kpc)	$T_{noise,\,150pc}$ (K)	$r_{ch,\,150pc}$	$f_{CO,\,150pc}$	$N_{los,\,150pc}$
(1)	(2)	(3)	(4)	(5)	(6)	(7)	(8)	(9)	(10)	(11)	(12)	(13)
NGC 5134	Y	N	18.5	22.7	311.6	21.6	0.37	4.2	0.047	0.059	59%	538
NGC 5248	?	Y	12.7	49.5	106.2	17.0	1.54	3.2	0.049	0.065	87%	1190
NGC 5530	?	N	11.8	61.9	305.4	9.4	0.31	2.8	0.046	0.057	70%	798
NGC 5643	Y	Y	11.8	29.9	318.7	18.2	2.14	3.5	0.034	0.058	83%	2667
NGC 6300	Y	N	13.1	49.3	105.5	29.2	2.39	4.0	0.050	0.059	81%	2120
NGC 6744	Y	Y	11.6	53.2	14.3	48.8	2.28	9.7	0.065	0.065	66%	2511
NGC 7456	?	N	7.94	63.7	12.9	1.2	0.06	2.2	0.011	0.057	48%	133
NGC 7496	Y	N	18.7	34.7	196.4	9.8	2.16	3.3	0.029	0.056	79%	1557

Notes. (2–3) If the galaxy has identifiable stellar bars and spiral arms (?—ambiguous; see M. Querejeta et al. 2020, in preparation); (4) distance (Tully et al. 2009); (5–6) galaxy inclination and position angle (Lang et al. 2020); (7–9) galaxy global stellar mass, SFR, and the effective (half-mass) radius estimated from the measured stellar scale length (Leroy et al. 2019; A. K. Leroy et al. 2020a, in preparation); (10–11) CO data rms noise and channel-to-channel correlation at 150 pc resolution; (12) CO flux completeness at 150 pc resolution; (13) number of independent sightlines at 150 pc resolution.

[a] These three very nearby galaxies are only observed by the ACA 7 m and total power telescopes. Because of their proximity, the data still have linear resolutions matched to the other galaxies in the sample.

[b] Measurements in these four galaxies are not presented in Section 3.

[c] The estimated CO flux completeness exceeds 100% for these two targets. This is due to either low-S/N data (NGC 4424) or calibration mismatch between the interferometric and single-dish data (NGC 1317).

(This table is available in machine-readable form.)

Appendix B
Data Product

We publish our measurements in a machine readable table and demonstrate its form and content in Table B1.

Table B1
Table of Key Measurements

Galaxy	Resolution (pc)	r_{gal} (kpc)	Center	Arm	Inter-arm	$I_{CO(2-1)}$ (K km s^{-1})	Σ_{mol} ($M_\odot$ pc^{-2})	σ_{mol} (km s^{-1})	P_{turb} (k_B K cm^{-3})	α_{vir}
(1)	(2)	(3)	(4)	(5)	(6)	(7)	(8)	(9)	(10)	(11)
Circinus	150	0.000	1	0	0	7.680e+02	3.423e+03	7.664e+01	6.574e+08	5.280e+00
Circinus	150	0.154	1	0	0	4.755e+02	2.161e+03	4.053e+01	1.160e+08	2.339e+00
Circinus	150	0.154	1	0	0	3.649e+02	1.659e+03	4.124e+01	9.228e+07	3.154e+00
Circinus	150	0.290	1	0	0	3.433e+02	1.596e+03	4.595e+01	1.101e+08	4.071e+00
Circinus	150	0.290	1	0	0	5.191e+02	2.398e+03	7.411e+01	4.305e+08	7.048e+00
Circinus	150	0.307	1	0	0	2.265e+02	1.053e+03	2.411e+01	2.001e+07	1.698e+00
Circinus	150	0.307	1	0	0	2.698e+02	1.252e+03	2.277e+01	2.121e+07	1.275e+00
Circinus	150	0.322	1	0	0	3.209e+02	1.493e+03	4.636e+01	1.049e+08	4.430e+00
Circinus	150	0.322	1	0	0	3.470e+02	1.624e+03	5.172e+01	1.420e+08	5.068e+00
Circinus	150	0.334	1	0	0	1.989e+02	9.334e+02	3.261e+01	3.244e+07	3.505e+00
…	…	…	…	…	…	…	…	…	…	…

(This table is available in its entirety in machine-readable form.)

Appendix C
Data Censoring Function

As mentioned in Section 2, our data cube masking scheme introduces a censoring effect that excludes sightlines with low I_{CO} and high σ_{CO}. Here we provide the analytic expression for this censoring function.

We consider a generic masking scheme requiring N consecutive channels with S/N $> X_{th}$. The intrinsic CO line profile is assumed to be Gaussian, with a peak brightness temperature of T_{peak} and a 1σ line width of σ_{CO}. We also assume the line peak is located right at the center of the N consecutive channels, each of which has a channel width v_{ch}. If the CO intensity in the "edge" channels (i.e., $\pm N/2$ channels away from the line center) exceeds $X_{th}\ T_{noise}\ v_{ch}$, then all channels in between also exceed this threshold, and thus this CO line should enter the signal mask. Following this argument, we can get an expression for the censoring function by integrating the line profile within that "edge" channel:

$$\int_{(N/2-1)v_{ch}}^{(N/2)v_{ch}} T_{peak} \exp(-v^2/2\sigma_{CO}^2) dv > X_{th}\ T_{noise}\ v_{ch}\ . \quad \text{(C1)}$$

Recasting this integral by the error function and re-expressing T_{peak} with line-integrated intensity $I_{CO} = \sqrt{2\pi}\ T_{peak}\ \sigma_{CO}$, we have

$$I_{CO} > \frac{1}{2} X_{th}\ T_{noise}\ v_{ch} \left[\mathrm{erf}\left(\frac{N}{2} \frac{v_{ch}}{\sqrt{2}\ \sigma_{CO}} \right) - \mathrm{erf}\left(\frac{N-2}{2} \frac{v_{ch}}{\sqrt{2}\ \sigma_{CO}} \right) \right]^{-1} . \quad \text{(C2)}$$

The above derivation assumes an infinitely sharp spectral response curve, which is inconsistent with the nonzero channel-to-channel correlation estimated for our data (see Table A1). To address this, we introduce a three-element Hann kernel of the shape $[k,\ 1\text{–}2k,\ k]$ to model the spectral response curve. Here the value k is determined so that the resultant channel-to-channel correlation matches the estimated r_{ch} for our data (following Equation (15) in Leroy et al. 2016). Convolving the left-hand side of Equation (C1) with this kernel and recasting the formula into a similar form as Equation (C2), we get a modified censoring function that accounts for the realistic spectral response curve[36]:

$$\begin{aligned} I_{CO} > \frac{1}{2} X_{th}\ T_{noise}\ v_{ch} \Bigg[& k \cdot \mathrm{erf}\left(\frac{N+2}{2} \frac{v_{ch}}{\sqrt{2}\ \sigma_{CO}} \right) \\ & + (1-3k) \cdot \mathrm{erf}\left(\frac{N}{2} \frac{v_{ch}}{\sqrt{2}\ \sigma_{CO}} \right) \\ & - (1-3k) \cdot \mathrm{erf}\left(\frac{N-2}{2} \frac{v_{ch}}{\sqrt{2}\ \sigma_{CO}} \right) \\ & - k \cdot \mathrm{erf}\left(\frac{N-4}{2} \frac{v_{ch}}{\sqrt{2}\ \sigma_{CO}} \right) \Bigg]^{-1} . \end{aligned} \quad \text{(C3)}$$

[36] The `Python` realization of this censoring function calculation is available at https://github.com/astrojysun/SpectralCubeTools.

Taking $N = 2$, $X_{th} = 2$, $v_{ch} = 2.5\ \mathrm{km\ s^{-1}}$, and the corresponding T_{noise} and k values for each galaxy in Equation (C3), we recover the censoring function shown in Figure 1.

ORCID iDs

Jiayi Sun (孙嘉懿) https://orcid.org/0000-0003-0378-4667
Adam K. Leroy https://orcid.org/0000-0002-2545-1700
Eva Schinnerer https://orcid.org/0000-0002-3933-7677
Annie Hughes https://orcid.org/0000-0002-9181-1161
Erik Rosolowsky https://orcid.org/0000-0002-5204-2259
Miguel Querejeta https://orcid.org/0000-0002-0472-1011
Daizhong Liu https://orcid.org/0000-0001-9773-7479
Toshiki Saito https://orcid.org/0000-0002-2501-9328
Cinthya N. Herrera https://orcid.org/0000-0001-6405-0785
Christopher Faesi https://orcid.org/0000-0001-5310-467X
Antonio Usero https://orcid.org/0000-0003-1242-505X
Jérôme Pety https://orcid.org/0000-0003-3061-6546
J. M. Diederik Kruijssen https://orcid.org/0000-0002-8804-0212
Eve C. Ostriker https://orcid.org/0000-0002-0509-9113
Frank Bigiel https://orcid.org/0000-0003-0166-9745
Guillermo A. Blanc https://orcid.org/0000-0003-4218-3944
Alberto D. Bolatto https://orcid.org/0000-0002-5480-5686
Médéric Boquien https://orcid.org/0000-0003-0946-6176
Mélanie Chevance https://orcid.org/0000-0002-5635-5180
Daniel A. Dale https://orcid.org/0000-0002-5782-9093
Sinan Deger https://orcid.org/0000-0003-1943-723X
Eric Emsellem https://orcid.org/0000-0002-6155-7166
Simon C. O. Glover https://orcid.org/0000-0001-6708-1317
Kathryn Grasha https://orcid.org/0000-0002-3247-5321
Brent Groves https://orcid.org/0000-0002-9768-0246
Jonathan Henshaw https://orcid.org/0000-0001-9656-7682
Maria J. Jimenez-Donaire https://orcid.org/0000-0002-9165-8080
Jenny J. Kim https://orcid.org/0000-0002-0432-6847
Ralf S. Klessen https://orcid.org/0000-0002-0560-3172
Kathryn Kreckel https://orcid.org/0000-0001-6551-3091
Janice C. Lee https://orcid.org/0000-0002-2278-9407
Sharon Meidt https://orcid.org/0000-0002-6118-4048
Karin Sandstrom https://orcid.org/0000-0002-4378-8534
Amy E. Sardone https://orcid.org/0000-0002-5783-145X
Dyas Utomo https://orcid.org/0000-0003-4161-2639
Thomas G. Williams https://orcid.org/0000-0002-0012-2142

References

Accurso, G., Saintonge, A., Catinella, B., et al. 2017, MNRAS, 470, 4750
Armillotta, L., Krumholz, M. R., di Teodoro, E. M., & McClure-Griffiths, N. M. 2019, MNRAS, 490, 4401
Astropy Collaboration, Price-Whelan, A. M., Sipőcz, B. M., et al. 2018, AJ, 156, 123
Blitz, L., & Rosolowsky, E. 2004, ApJL, 612, L29
Bolatto, A. D., Leroy, A. K., Rosolowsky, E., Walter, F., & Blitz, L. 2008, ApJ, 686, 948
Chevance, M., Kruijssen, J. M. D., Hygate, A. P. S., et al. 2020, MNRAS, 493, 2872
Colombo, D., Hughes, A., Schinnerer, E., et al. 2014a, ApJ, 784, 3
Colombo, D., Meidt, S. E., Schinnerer, E., et al. 2014b, ApJ, 784, 4
Colombo, D., Rosolowsky, E., Duarte-Cabral, A., et al. 2019, MNRAS, 483, 4291
den Brok, J. S., Chatzigiannakis, D., Bigiel, F., et al. 2020, MNRAS, submitted
Dobbs, C. L., & Bonnell, I. A. 2008, MNRAS, 385, 1893
Dobbs, C. L., Rosolowsky, E., Pettitt, A. R., et al. 2019, MNRAS, 485, 4997
Donovan Meyer, J., Koda, J., Momose, R., et al. 2013, ApJ, 772, 107

Egusa, F., Hirota, A., Baba, J., & Muraoka, K. 2018, ApJ, 854, 90
Elmegreen, B. G. 1989, ApJ, 338, 178
Field, G. B., Blackman, E. G., & Keto, E. R. 2011, MNRAS, 416, 710
Fujimoto, Y., Chevance, M., Haydon, D. T., Krumholz, M. R., & Kruijssen, J. M. D. 2019, MNRAS, 487, 1717
Gensior, J., Kruijssen, J. M. D., & Keller, B. W. 2020, MNRAS, 495, 199
Ginsburg, A., Koch, E., Robitaille, T., et al. 2019, radio-astro-tools/spectral-cube, v0.4.5, Zenodo, doi:10.5281/zenodo.3558614
Henshaw, J. D., Kruijssen, J. M. D., Longmore, S. N., et al. 2020, NatAs, in press (doi:10.1038/s41550-020-1126-z)
Henshaw, J. D., Longmore, S. N., Kruijssen, J. M. D., et al. 2016, MNRAS, 457, 2675
Herrera-Endoqui, M., Díaz-García, S., Laurikainen, E., & Salo, H. 2015, A&A, 582, A86
Heyer, M. H., Carpenter, J. M., & Snell, R. L. 2001, ApJ, 551, 852
Hirota, A., Egusa, F., Baba, J., et al. 2018, PASJ, 70, 73
Hughes, A., Meidt, S. E., Colombo, D., et al. 2013a, ApJ, 779, 46
Hughes, A., Meidt, S. E., Schinnerer, E., et al. 2013b, ApJ, 779, 44
Jeffreson, S. M. R., & Kruijssen, J. M. D. 2018, MNRAS, 476, 3688
Jeffreson, S. M. R., Kruijssen, J. M. D., Keller, B. W., Chevance, M., & Glover, S. C. O. 2020, MNRAS, 498, 385
Jogee, S., Scoville, N., & Kenney, J. D. P. 2005, ApJ, 630, 837
Kruijssen, J. M. D., Longmore, S. N., Elmegreen, B. G., et al. 2014, MNRAS, 440, 3370
Lada, C. J., & Dame, T. M. 2020, ApJ, 898, 3
Lang, P., Meidt, S. E., Rosolowsky, E., et al. 2020, ApJ, 897, 122
Leroy, A. K., Hughes, A., Schruba, A., et al. 2016, ApJ, 831, 16
Leroy, A. K., Lee, C., Schruba, A., et al. 2013a, ApJL, 769, L12
Leroy, A. K., Sandstrom, K. M., Lang, D., et al. 2019, ApJS, 244, 24
Leroy, A. K., Walter, F., Sandstrom, K., et al. 2013b, AJ, 146, 19
McMullin, J. P., Waters, B., Schiebel, D., Young, W., & Golap, K. 2007, in ASP Conf. Ser. 376, Astronomical Data Analysis Software and Systems XVI, ed. R. A. Shaw, F. Hill, & D. J. Bell (San Francisco, CA: ASP), 127
Meidt, S. E., Glover, S. C. O., Kruijssen, J. M. D., et al. 2020, ApJ, 892, 73
Meidt, S. E., Leroy, A. K., Rosolowsky, E., et al. 2018, ApJ, 854, 100
Miville-Deschênes, M.-A., Murray, N., & Lee, E. J. 2017, ApJ, 834, 57
Ostriker, E. C., McKee, C. F., & Leroy, A. K. 2010, ApJ, 721, 975
Pfenniger, D., & Norman, C. 1990, ApJ, 363, 391
Rice, T. S., Goodman, A. A., Bergin, E. A., Beaumont, C., & Dame, T. M. 2016, ApJ, 822, 52
Roman-Duval, J., Heyer, M., Brunt, C. M., et al. 2016, ApJ, 818, 144
Rosolowsky, E., & Leroy, A. 2006, PASP, 118, 590
Sakamoto, K., Okumura, S. K., Ishizuki, S., & Scoville, N. Z. 1999, ApJ, 525, 691
Salo, H., Laurikainen, E., Laine, J., et al. 2015, ApJS, 219, 4
Sánchez, S. F., Barrera-Ballesteros, J. K., López-Cobá, C., et al. 2019, MNRAS, 484, 3042
Sánchez, S. F., Rosales-Ortega, F. F., Iglesias-Páramo, J., et al. 2014, A&A, 563, A49
Sandstrom, K. M., Leroy, A. K., Walter, F., et al. 2013, ApJ, 777, 5
Sawada, T., Hasegawa, T., & Koda, J. 2012, ApJL, 759, L26
Schruba, A., Kruijssen, J. M. D., & Leroy, A. K. 2019, ApJ, 883, 2
Semenov, V. A., Kravtsov, A. V., & Gnedin, N. Y. 2018, ApJ, 861, 4
Sheth, K., Vogel, S. N., Regan, M. W., et al. 2002, AJ, 124, 2581
Sormani, M. C., Treß, R. G., Glover, S. C. O., et al. 2019, MNRAS, 488, 4663
Sun, J., Leroy, A. K., Ostriker, E. C., et al. 2020, ApJ, 892, 148
Sun, J., Leroy, A. K., Schruba, A., et al. 2018, ApJ, 860, 172
Tress, R. G., Smith, R. J., Sormani, M. C., et al. 2020a, MNRAS, 492, 2973
Tress, R. G., Sormani, M. C., Glover, S. C. O., et al. 2020b, MNRAS, submitted (arXiv:2004.06724)
Tully, R. B., Rizzi, L., Shaya, E. J., et al. 2009, AJ, 138, 323